Uncertainties in temperature statistics and fluxes determined by sonic anemometer due to wind-induced vibrations of mounting arms

Zhongming Gao[1,2,3], Heping Liu[3,*], Dan Li[4], Bai Yang[5], Von Walden[3], Lei Li[1,2], Ivan Bogoev[5]

[1] School of Atmospheric Sciences, Sun Yat-sen University, Southern Marine Science and Engineering Guangdong Laboratory (Zhuhai), Zhuhai, China

[2] Key Laboratory of Tropical Atmosphere-Ocean System, Ministry of Education, Sun Yat-sen University, Zhuhai, Guangdong, China

[3] Laboratory for Atmospheric Research, Department of Civil and Environmental Engineering, Washington State University, Pullman, Washington, USA

[4] Department of Earth and Environment, Boston University, Boston, Massachusetts, USA

[5] Campbell Scientific, Inc., Logan, Utah, USA

*Corresponding to: Heping Liu (heping.liu@wsu.edu)

Abstract

Accurate air temperature measurements are essential in eddy covariance systems, not only for determining sensible heat flux but also for applying the density effect corrections (DEC) to water vapor and CO_2 fluxes. However, the influence of wind-induced vibrations of mounting structures on temperature fluctuations remains a subject of investigation. This study examines 30-min average temperature variances and fluxes using eddy covariance systems, combining Campbell Scientific Anemometer Thermometry (CSAT3B) with closely co-located fine-wire thermocouples alongside LI-COR CO_2/H_2O gas analyzers at multiple heights above a sagebrush ecosystem. The variances of sonic temperature after humidity corrections (T_s) and sensible heat fluxes derived from T_s are underestimated (e.g., by approximately 5% for temperature variances and 4% for sensible heat fluxes at 40.2 m, respectively) as compared with those measured by a fine-wire thermocouple (T_c). Spectral analysis illustrates that these underestimated variances and

fluxes are caused by the lower energy levels in the T_s spectra than the T_c spectra in the low frequency range (natural frequency < 0.02 Hz). This underestimated T_s spectra in the low frequency range become more pronounced with increasing as wind speeds, especially when wind speed exceeds 10 m s^{-1}. Moreover, the underestimated temperature variances and fluxes cause overestimated water vapor and CO_2 fluxes through DEC. Our analysis suggests that these underestimations when using T_s are likely due to wind-induced vibrations affecting the tower and mounting arms, altering the time of flight of ultrasonic signals along three sonic measurement paths. This study underscores the importance of further investigations to develop corrections for these errors.

Keywords: Eddy covariance, CO₂ fluxes, Fine-wire thermocouple, Sonic temperature; High winds

1. Introduction

The eddy covariance (EC) technique has been widely used to measure turbulent fluxes of heat, water vapor, CO_2, and other scalars between terrestrial ecosystems and the atmosphere (Chu et al., 2021; Lee et al., 2014; Missik et al., 2021; Tang et al., 2019; Wang et al., 2010). It is instrumental in studying micrometeorological processes in the atmospheric surface layer (Eder et al., 2013; Gao et al., 2018; Guo et al., 2009; Li et al., 2018; Zhang et al., 2010). Despite considerable advancement in the EC technique (Burns et al., 2012; Frank et al., 2013; Fratini et al., 2012; Horst et al., 2015; Liu et al., 2001; Mauder et al., 2007; Mauder and Zeeman, 2018; Wilczak et al., 2001), uncertainties in EC fluxes remain a great concern (Loescher et al., 2005; Massman and Clement, 2006; Peña et al., 2019), including the notable issue of the surface energy balance closure (Mauder et al., 2020). Thus, improving the accuracy of EC flux measurements and identifying the potential sources of uncertainties in these fluxes are critically important.

In most EC applications, sonic-derived air temperature after corrections is usually employed for determining sensible heat fluxes (H) (Liu et al., 2001; Schotanus et al., 1983). However, erroneous H determined by sonic anemometers have been reported especially under high wind conditions (e.g., Burns et al., 2012; Smedman et al., 2007). For instance, Smedman et al. (2007) utilizing two co-located Gill sonic anemometers (Models R2 and R3) observed that sonic-

62   determined H exhibited larger magnitudes than H measured with an alternative temperature sensor.

63   They also noted that for wind speed exceeding 10 m s^{-1}, a correction highly dependent on wind

64   speed is essential for sonic-determined H (Smedman et al., 2007). Burns et al. (2012), employing

65   a Campbell Scientific sonic anemometer (Model CSAT3) and a co-located type-E thermocouple

66   (wire diameter of 0.254 mm), reported substantial errors for H determined from the CSAT3 sonic

67   anemometer with a firmware of version 4.0 for wind speed above 8 m s^{-1}. Such large errors in H

68   result from inaccurate sonic-derived temperature due to an underestimation of the speed of sound,

69   though errors caused by sonic anemometer transducer shadowing can also cause errors in H (Frank

70   et al., 2013; Horst et al., 2015). Wind-induced vibrations in the tower and mounting arms,

71   particularly under windy conditions, were speculated to be potential contributors, causing spikes

72   in the signals of sonic temperature (Burns et al., 2012). However, the precise impact of vibration-

73   induced errors in sonic-derived temperature on temperature variances and sensible heat fluxes,

74   especially for tall towers under strong wind conditions, has remained unexplored.

75   Accurate air temperature measurements are not only important for determining H but also

76   crucial for estimating other scalar fluxes (e.g., water vapor and CO_2) through density effect

77   corrections (DEC hereafter; Detto and Katul, 2007; Gao et al., 2020; Lee and Massman, 2011;

78   Sahlée et al., 2008; Webb et al., 1980). The measured high-frequency time series of densities of

79   water vapor, CO_2, and other scalars are subjected to the effects of density fluctuations of dry air

80   and other components in the atmosphere, as well as the fluctuations of air pressure (Lee and

81   Massman, 2011; Webb et al., 1980). Correcting for these effects involves applying corrections to

82   either the calculated raw fluxes or to the high-frequency time series of the scalar density

83   fluctuations (Webb et al., 1980; Detto and Katul, 2007; Gao et al., 2020; Sahlée et al., 2008). Any

84   errors or uncertainties in sonic-derived temperature are anticipated to propagate, and in some

85   certain cases, be amplified by the correction algorithms applied to the scalar fluxes, leading to

86   heightened uncertainties in these fluxes (Liu et al., 2006).

87   The objective of this study Is to scrutinize the uncertainties in temperature statistics and

88   fluxes determined by sonic anemometers, with particular attention to the potential influence of

89   vibrations of the tower and mounting arms under high wind speeds. The data employed were

90   collected from three levels of Campbell Scientific sonic anemometers (Model CSAT3B) alongside

91   co-located fine wire thermocouples and open-path infrared gas analyzers. By comparing the

92   sensible heat fluxes calculated using air temperature from the sonic anemometers and the

93 thermocouples, we assess vibration-induced errors in sensible heat fluxes at the three heights. The

94 findings reveal that the sonic anemometers underestimate the temperature variances and fluxes

95 compared to the thermocouples. Furthermore, we investigate the propagation of these vibration-

96 induced errors to water vapor and CO_2 fluxes through the density effect corrections.

97

98 **2. Materials and methods**

99 **2.1 Experiment and data**

100 The experiment was conducted at the National Oceanic and Atmospheric Administration

101 (NOAA) Grid 3 area (Station ID: GRI) situated on the western edge of the Snake River Plain in

102 southeastern Idaho, USA (43.59°N, 112.94°W; 1,500 m above mean sea level; Figure 1). The

103 closest mountains are located approximately 13 km northwest from GRI. Based on the data from

104 multiple automated meteorological observation stations in the area, southwesterly and

105 northeasterly winds prevail during the day and night, respectively (Finn et al., 2016). Under these

106 prevailing winds, GRI has a relatively flat and uniform upwind fetch (Finn et al., 2018; Lan et al.,

107 2018). The vegetation primarily comprises shrubs and grasses, each with a roughness length and

108 displacement height of a few centimeters (Finn et al., 2016).

109 The experiment utilized a 62-m tower and a 10-m aluminum tower (UT30, Campbell

110 Scientific, Inc.) at the Grid 3 area to mount the sensors (Figure 1). The 62-m tower was guyed at

111 eight levels and the 10-m tower was guyed at one level. 3.6 m (12-ft) retractable square booms

112 were horizontally braced to the 62-m tower to attach the sensors. The CSAT3s and IRGAs were

113 mounted on 1-ft pipes, which were securely attached to the end of each boom. As a result, the

114 CSAT3s and IRGAs were positioned at least 2.0 m away from the tower structure. On the 10-m

115 tower, 1.8 m (6-ft) poles were utilized to mount the CSAT3s and IRGAs, positioning the sensors

116 approximately 1.5 m away from the tower's frame structures.
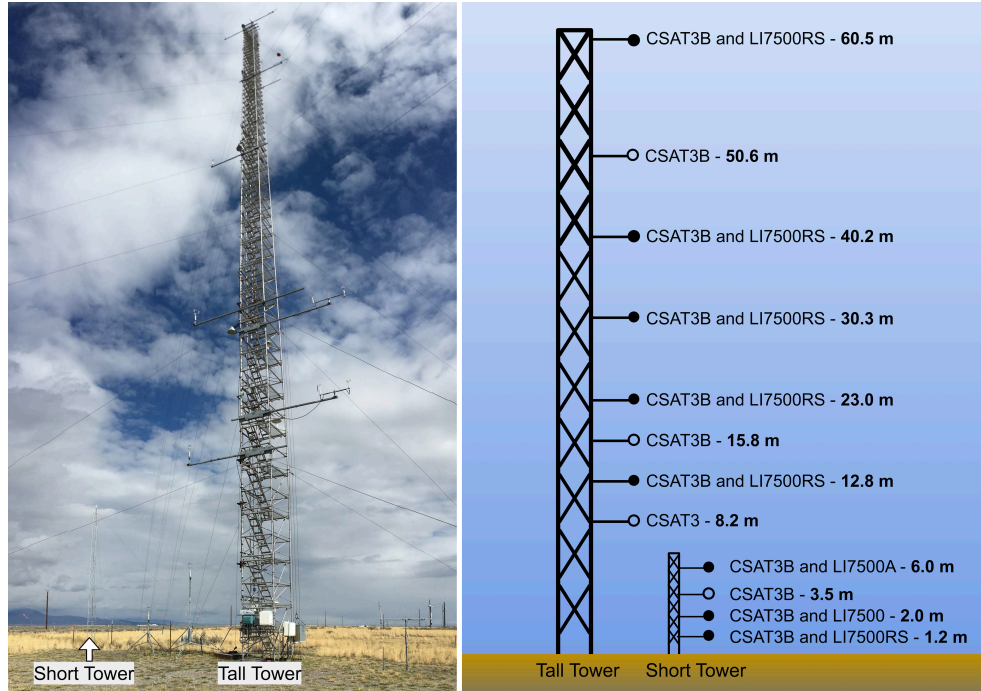
Figure 1. Photos of the 62-m and 10-m towers at the Idaho National Laboratory (INL) site in southeastern Idaho, and the instrumentational configuration of the field study.

Throughout the experiment, multiple levels of EC systems were deployed (Figure 1). These EC systems included two models of 3D sonic anemometers from the same manufacturers (Model CSAT3B and CSAT3, Campbell Scientific, Inc.) and three models of infrared gas analyzers from the same manufacturers (IRGA; Model LI7500RS, LI7500A, and LI7500, LICOR, Inc.). CSAT3s measured the three-dimensional wind velocity components (u, v, and w) and the sonic air temperature (T_{s_m}), while IRGAs measured the densities of water vapor (ρ_v) and CO_2 (ρ_c). Co-located with CSAT3s and IRGAs, Type-E fine wire thermocouples (Model FW3, Campbell Scientific, Inc.) were used to measure air temperature (T_c) at six heights of 2.0 m, 8.2 m, 12.8m, 15.8 m, 23.0 m, and 40.2 m. FW3 thermocouple is composed of a chromel wire and a constantan wire with diameters of 0.0762 mm. The FW3 determines T_c by measuring the voltage potential differences created at the junction of the two wires due to the temperature difference, whereas T_{s_m} is determined based on the relationship between sonic virtual temperature and the speed of sound (Liu et al., 2001). This distinction in temperature measurement principles between CSAT3s and FW3 implies that the measured T_{s_m} and T_c are independent of each other. Furthermore, T_c is expected to remain unaffected by vibrations of the tower and mounting arms. In this study, we also

136   recorded the inclination of the CSAT3B (e.g., pitch and roll angle measurements) given by an

137   integrated inclinometer in the CSAT3B. Pitch angle is defined as the angle between the

138   gravitationally horizontal plane and the CSAT3B x-axis, and roll angle is defined as the angle

139   between the gravitationally horizontal plane and the CSAT3B y-axis. The sonic roll and pitch

140   angles were stored as 30-min averages.

141   Three dataloggers (Model CR1000X, Campbell Scientific, Inc.) were employed to sample

142   the high-frequency instruments (i.e., sonic anemometer, fine-wire thermocouple, and gas analyzer)

143   at 10 Hz. Each datalogger was equipped with a GPS receiver (Model GPS16X-HVS, Garmin

144   International, Inc.) to synchronize the datalogger clocks. Additionally, a variety of meteorological

145   measurements were conducted at GRI, including net radiation, air temperature, relative humidity,

146   soil moisture, soil temperature, and soil heat fluxes. In this study, we examined the data collected

147   at three different heights (40.2 m, 23.0 m, and 12.8 m) from 25 April to 31 July 2021, considering

148   structural differences between the tall tower and short tower setups as well as potential influences

149   from the roughness sublayer on measurement at lower levels.

150

151   **2.2 Post-field data processing**

152   The data processing mainly entailed despiking, double rotation for the wind components

153   (Wilczak et al., 2001), sonic temperature conversion (Liu et al., 2001; Schotanus et al., 1983), and

154   application of DEC to the raw fluxes of latent heat and CO_2 (Webb et al., 1980). However,

155   corrections for the effects of humidity and density fluctuations in this study are applied to the

156   turbulent fluctuations of sonic temperature, ρ_v, and ρ_c, respectively (Detto and Katul, 2007; Gao

157   et al., 2020; Sahlée et al., 2008; Schotanus et al., 1983; Webb et al., 1980). For each 30-min

158   interval, the corrected turbulent fluctuations of sonic temperature (T_s'), ρ_v', and ρ_c' are determined

159   by,

$$T_s'(t) = T_{s\_m}'(t) - 0.51 \frac{\rho_v'(t)}{\bar{\rho}_a} \bar{T}, \tag{1}$$

$$\rho_v'(t) = (1 + \mu\sigma)\rho_{v\_m}'(t) + (1 + \mu\sigma)\frac{\bar{\rho}_v}{\bar{T}} T_s'(t), \tag{2}$$

$$\rho_c'(t) = \rho_{c\_m}'(t) + \bar{\rho}_c(1 + \mu\sigma)\frac{T_s'(t)}{\bar{\bar{T}}} + \mu\frac{\bar{\rho}_c}{\bar{\rho}_a}\rho_v'(t). \tag{3}$$

160   where T_{s_m}, ρ_{v_m}, and ρ_{c_m} represent measured sonic temperature, water vapor and CO_2 densities,

161 respectively; $\bar{T}$, $\bar{\rho}_a$, $\bar{\rho}_v$, and $\bar{\rho}_c$ are averages of air temperature, air density, water vapor and CO_2

162 densities, respectively; $\mu = m_d/m_v$ (m_d and m_v are the molecular mass of dry air and water

163 vapor, respectively); $\sigma = \bar{\rho}_v/\bar{\rho}_d$ ($\bar{\rho}_d$ is the density of dry air). The prime symbol denotes the

164 turbulent fluctuations relative to the 30-min block average. As shown in the equations above, there

165 is interdependence between T_s' and ρ_v', and thus T_s' and ρ_v' must be determined iteratively. In this

166 study, the corrections are iterated twice. Note that in semiarid sites like ours, the adjustments to T_s'

167 due to fluctuations in specific humidity ($\frac{\rho_v'(t)}{\bar{\rho}_a}$) are typically negligible (not shown here) as

168 compared to the adjustment to ρ_v' due to fluctuations in T_s' (as demonstrated in Section 3.5). The

169 corrected time series of fluctuations facilitate the investigation of coherent structures and scalar

170 similarity between temperature and other scalars (Detto and Katul, 2007; Sahlée et al., 2008). Here

171 and throughout, T_s refers to the air temperature measured by sonic anemometers after humidity

172 corrections, T_{s_m} the sonic temperature directly measured before corrections, and T_c the air

173 temperature measured by fine-wire thermocouples (FW3).

174

175 **2.3 Ensemble empirical mode decomposition (EEMD)**

176   The ensemble empirical mode decomposition (EEMD) (Huang et al., 1998; Huang and Wu,

177 2008) is applied to decompose the 30-min turbulence time series into three subsequences,

178 corresponding to the high, middle, and low frequency ranges, respectively. EEMD is a favored

179 method in analyzing non-linear and non-stationary turbulence data (Gao et al., 2018; Hong et al.,

180 2010; Liu et al., 2021; Huang et al., 1998; Huang and Wu, 2008). Through the sifting process in

181 EEMD, a 30-min time series is decomposed into thirteen oscillatory components $C_j(t)$ (j = 1, 2, …,

182 13) and an overall residual $r_{13}(t)$. Each oscillatory component generally exhibits one

183 characteristic frequency (Hong et al., 2010; Gao et al., 2018), while the overall residual is either

184 monotonic or containing only one extremum, from which no more oscillatory components can be

185 further decomposed. Hence,

$$x(t) = r_{13}(t) + \sum_{j=1}^{13} C_j(t). \tag{4}$$

186   As detailed in Section 3.2, after comparing the power spectra of T_s and T_c, two frequency

187 boundaries, 0.02 and 0.2 Hz, are identified. The oscillatory components are then categorized into

188 three frequency ranges (I, II, and III, respectively). The oscillatory components with mean

189 frequencies falling within the corresponding ranges are added together to generate the three

190 subsequences. Specifically, oscillatory components with the mean frequencies smaller than 0.02

191 Hz are summed and labeled as regime I (i.e., $x_I' = \sum_{j=10}^{13} C_{j,x} + r_{13}$, where $x = w, T_s,$ and T_c),

192 between 0.02 Hz and 0.2 Hz as regime II (i.e., $x_{II}' = \sum_{j=6}^{9} C_{j,x}$), and larger than 0.2 Hz as regime

193 III (i.e., $x_{III}' = \sum_{j=1}^{5} C_{j,x}$).

194

3 Results and discussion

3.1 Comparison of the CSAT3B- and FW3-derived temperature variances and fluxes

197 Figure 2 illustrates the comparisons between the variances and fluxes obtained using T_s

198 and T_c at different heights. Here, we use $\sigma_{T_c}^2$ and $\overline{w'T_c'}$ as reference values since T_c is less sensitive

199 to the effects of humidity and wind speeds than T_s (Burns et al., 2012; Smedman et al., 2007).

200 Generally, the variances of T_s ($\sigma_{T_s}^2$) are smaller than variances of T_c ($\sigma_{T_c}^2$), typically by 2%–5%

201 (Figures 2a-2c). These lower variances result in a lower sensible heat flux ($\overline{w'T_s'}$). Specifically, at

202 23.0 and 40.2 m, $\overline{w'T_s'}$ is underestimated by approximately 2% and 4%, respectively, as compared

203 to the sensible heat fluxes derived from the FW3 (i.e., $\overline{w'T_c'}$) (Figures 2d and 2e). However, at 12.8

204 m, $\overline{w'T_s'}$ and $\overline{w'T_c'}$ are quite comparable (Figure 2f). These results confirm that errors in H were

205 not entirely due to errors in the vertical velocity (Frank et al., 2013; Horst et al., 2015). Further

206 examination of Figure 2 reveals that the differences between $\sigma_{T_s}^2$ and $\sigma_{T_c}^2$, as well as between $\overline{w'T_s'}$

207 and $\overline{w'T_c'}$, increase with the increasing measurement heights. Additionally, our tests indicate that

208 the influence of solar heating on measurements of FW3 is negligible, primarily due to the thin wire

209 diameter of 0.0762 mm (Text S1 and Figure S1).
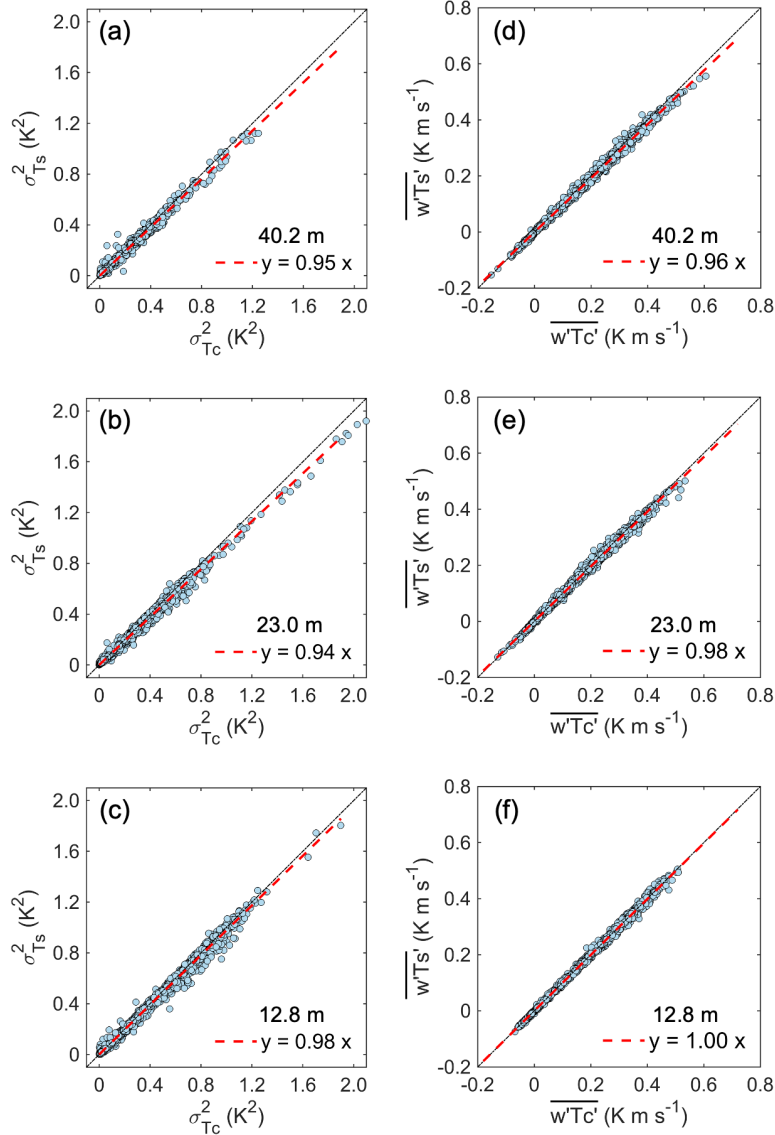
Figure 2. Comparison of temperature variances and sensible heat fluxes computed using T_s and T_c at the heights of 40.2, 23.0 and 12.8 m, respectively.

What mechanisms could have caused the observed differences? Previous studies found that CSAT3 sonic anemometers with a previous version of firmware could cause errors in T_s (Burns et al., 2012). However, this should not be the case for our study because the CSAT3B modes were used at these heights, and they have an improved design compared to the original CSAT3. Our results suggest that the differences are dependent on the measurement heights. As the measurement heights increase, the dominant length scale of coherent structures is also enlarged (Zhang et al.,

220   2011). Therefore, we conjecture that the processes that lead to such differences are most likely

221   scale dependent, motivating us to examine the spectra and cospectra in the next subsection.

222

223   **3.2 Spectral comparisons**

224   To gain further insight into the differences between $\sigma_{T_s}^2$ and $\sigma_{T_c}^2$ as well as the associated

225   fluxes (i.e., $\overline{w'T_s'}$ and $\overline{w'T_c'}$), the spectra of u, w, T_s and T_c and the w-T_s and w-T_c cospectra at

226   different heights are examined. Figures 3a-3c show the mean normalized Fourier power spectra of

227   u, w, T_s, and T_c as a function of natural frequency (f). Note that the power spectra were computed

228   every half hour using fast Fourier transform and normalized by the corresponding variances before

229   averaging. It is also interesting to note that the u, w, and T_s spectra deviate from the well-known

230    $-5/3$ power law in the high frequency range of $f > 0.2$ Hz, exhibiting similar features as previous

231   studies (e.g., Burns et al., 2012). For $f > 2$ Hz, fS_u, fS_w, and fS_{Ts} appear to follow the f^{+1} slope,

232   likely due to white noise and/or aliasing (Kaimal and Finnigan, 1994). In the 0.2 Hz $< f <$ 2 Hz

233   range, the distortion of fS_u, fS_w, and fS_{Ts} from the $-5/3$ power law is enhanced as the

234   measurement heights decrease. The upturned distortion for 0.2 Hz $< f <$ 2 Hz might be associated

235   with spikes (Gao et al., 2020; Stull, 1988) that are not excluded from the 10 Hz time series during

236   despiking. The T_c spectra appear to follow the $-5/3$ power law for 0.2 Hz $< f <$ 1 Hz, although are

237   slightly attenuated for $f > 1$ Hz, likely because the thermal mass of the thermocouple wire limits

238   its response time (Burns et al., 2012).
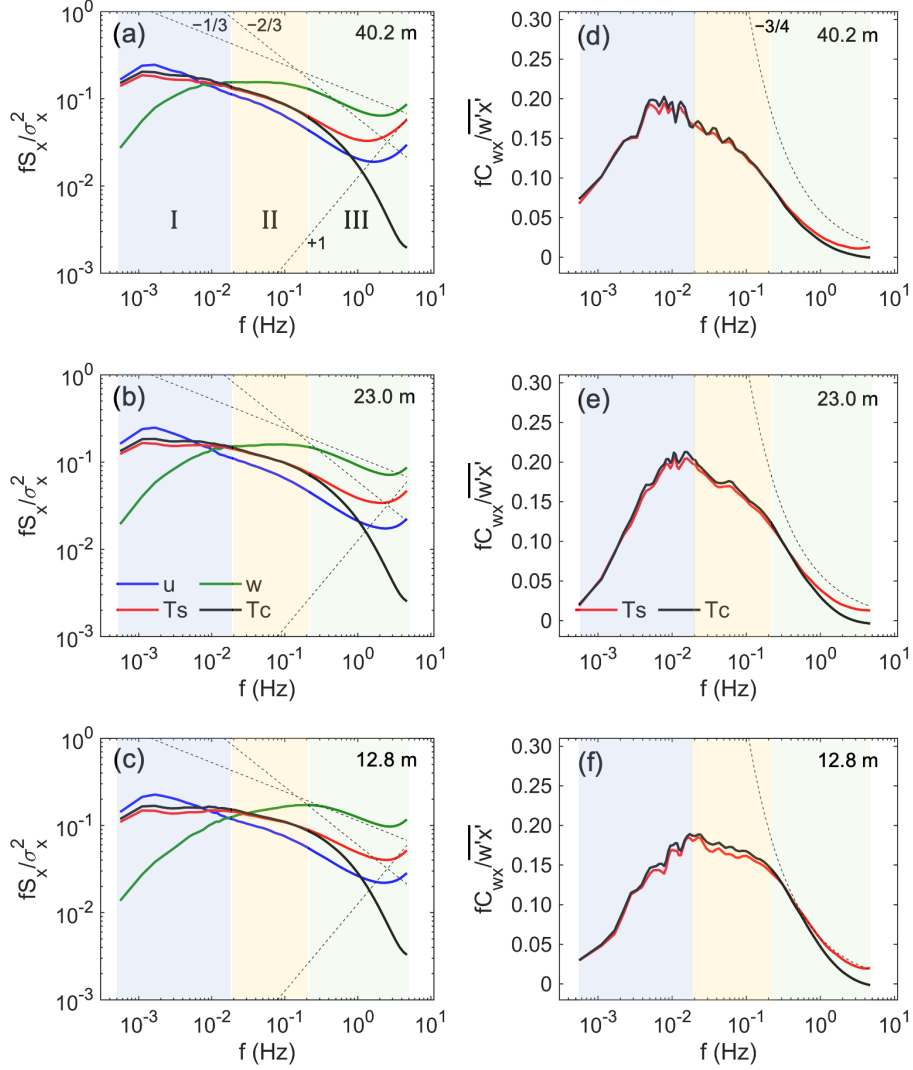
239

Figure 3. Mean normalized power spectra of u, w, T_s, and T_c, and cospectra of the w-T_s, and w-T_c, at three heights of 40.2, 23.0, and 12.8 m, respectively. All power spectra and cospectra are normalized by the corresponding variance and covariance before averaging. The dashed lines show a $f^{-1/3}$, $f^{-2/3}$, f^{+1}, and $f^{-3/4}$ slope. Note that the frequency domain can be divided into three regions by comparing the T_s and T_c spectra.

It is also noted that the magnitude of the T_c spectra is higher than that of the T_s spectra in the low frequency range of $f < 0.02$ Hz, but their magnitude is comparable in the middle frequency range of 0.02 Hz $< f < 0.2$ Hz. These results indicate that turbulent eddies with scales less than 0.02 Hz contribute more to $\sigma_{T_c}^2$ than $\sigma_{T_s}^2$. Hence, the underestimation of $\sigma_{T_s}^2$ is mostly caused by the

250   lower magnitude of the T_s spectra in the low frequency range, whereas $\sigma_{T_s}^2$ is overestimated to

251   some extent due to the upturned distortion of the T_s spectra in the high frequency range.

252   Figures 3d-3f show the distribution of the mean normalized w-T_s and w-T_c cospectra as a

253   function of f. Each cospectra is normalized by the corresponding covariances before averaging.

254   For $f > 0.2$ Hz, especially when $f > 0.5$ Hz, the w-T_s cospectra are generally higher than the w-

255   T_c cospectra, consistent with the higher spectra of T_s. Compared to the power law of $-3/4$, the

256   calculated $\overline{w'T_s'}$ are overestimated, while $\overline{w'T_c'}$ is slightly underestimated. For 0.002 Hz $< f < 0.2$

257   Hz, the normalized w-T_s cospectra are slightly lower than the normalized w-T_c cospectra,

258   indicating that turbulent eddies with scales in the frequency range of 0.002 Hz $< f < 0.2$ Hz

259   contribute more to $\overline{w'T_c'}$. Overall, the underestimation of the CSAT3B-derived fluxes is also scale-

260   dependent, and the underestimation of $\overline{w'T_s'}$ in the middle to low frequency range is offset by the

261   overestimation in the high frequency range to some extent.

262   According to the comparison of the T_s and T_c spectra, the whole frequency domain can be

263   divided into three ranges: I) $f < 0.02$ Hz, II) 0.02 Hz $< f < 0.2$ Hz, and III) $f > 0.2$ Hz. For $f <$

264   0.02 Hz, the magnitude of the T_c power spectra is slightly higher than that of the T_s spectra at all

265   levels, but the magnitude of the T_s and T_c spectra is comparable in the middle frequency range of

266   0.02 Hz $< f < 0.2$ Hz. For $f > 0.2$ Hz, the T_c spectra first follow the $-5/3$ power law and are then

267   attenuated, whereas the T_s spectra are distorted upward. Based on this division, in section 3.3, the

268   30-min time series is divided into the three frequency ranges and the contributions of these

269   different scales to $\sigma_{T_s}^2$, $\sigma_{T_c}^2$, $\overline{w'T_s'}$, and $\overline{w'T_c'}$ at different heights are then quantified.

270

271   **3.3 Scale-dependent contributions to variances and fluxes**

272   To quantify the contributions of different scales to the corresponding temperature variances

273   and fluxes, we apply the EEMD approach to decompose the 30-min time series of w', T_s', and T_c'

274   into various oscillatory components, which are then categorized into the three frequency ranges

275   discussed earlier (i.e., I, II, and III). Figures 4a-4c depict that for regime I, the ratios between the

276   variances of T_s and T_c are generally lower than 1.0 (approximately 0.89 on average). This suggests

277   that turbulent eddies with scales less than 0.02 Hz contribute approximately 11% more to $\sigma_{T_{c,I}}^2$

278   than $\sigma_{T_{s,I}}^2$. With these turbulent eddies contributing about 41%–57% to the total variances (Figures

279   5a-5c and Table 1), the 11% difference between $\sigma_{T_{c,I}}^2$ and $\sigma_{T_{s,I}}^2$ would cause 4%–6% difference

280 between the total variances of T_s and T_c. As for fluxes, turbulent eddies with scales less than 0.02

281 Hz contribute approximately 6% more to $\overline{w'T_s'}_I$ than $\overline{w'T_c'}_I$. With these turbulent eddies

282 accounting for about 26%–45% of the total fluxes (Figures 5d-5f and Table 1), the 6% difference

283 in $\overline{w'T_s'}_I$ and $\overline{w'T_c'}_I$ would cause 2%–3% difference in the total fluxes. Further, given that the

284 contribution of regime I to the total temperature variances and fluxes increases with measurement

285 height (Figure 5 and Table 1), the underestimation becomes more significant at higher levels.

286

287 **Table 1.** Contributions of the three frequency ranges to the total temperature variances and fluxes

288 of T_s and T_c, as well as the mean ratios of temperature variances and fluxes of T_s and T_c for each

289 range.

		40.2 m	23.0 m	12.8 m
$\sigma_{Ts,i}^2 / \sigma_{Ts}^2$	I	0.51	0.46	0.41
	II	0.32	0.36	0.37
	III	0.17	0.18	0.22
$\sigma_{Tc,i}^2 / \sigma_{Tc}^2$	I	0.57	0.52	0.47
	II	0.34	0.36	0.38
	III	0.10	0.12	0.15
$\sigma_{Ts,i}^2 / \sigma_{Tc,i}^2$	I	0.89	0.88	0.89
	II	0.98	0.98	0.99
	III	1.49	1.42	1.44
$\overline{w'Ts'}_i / \overline{w'Ts'}$	I	0.43	0.34	0.26
	II	0.42	0.47	0.48
	III	0.14	0.19	0.26
$\overline{w'Tc'}_i / \overline{w'Tc'}$	I	0.45	0.36	0.27
	II	0.43	0.48	0.50
	III	0.12	0.16	0.23
$\overline{w'Ts'}_i / \overline{w'Tc'}_i$	I	0.94	0.94	0.95
	II	0.98	0.99	0.99
	III	1.17	1.23	1.19

290

291
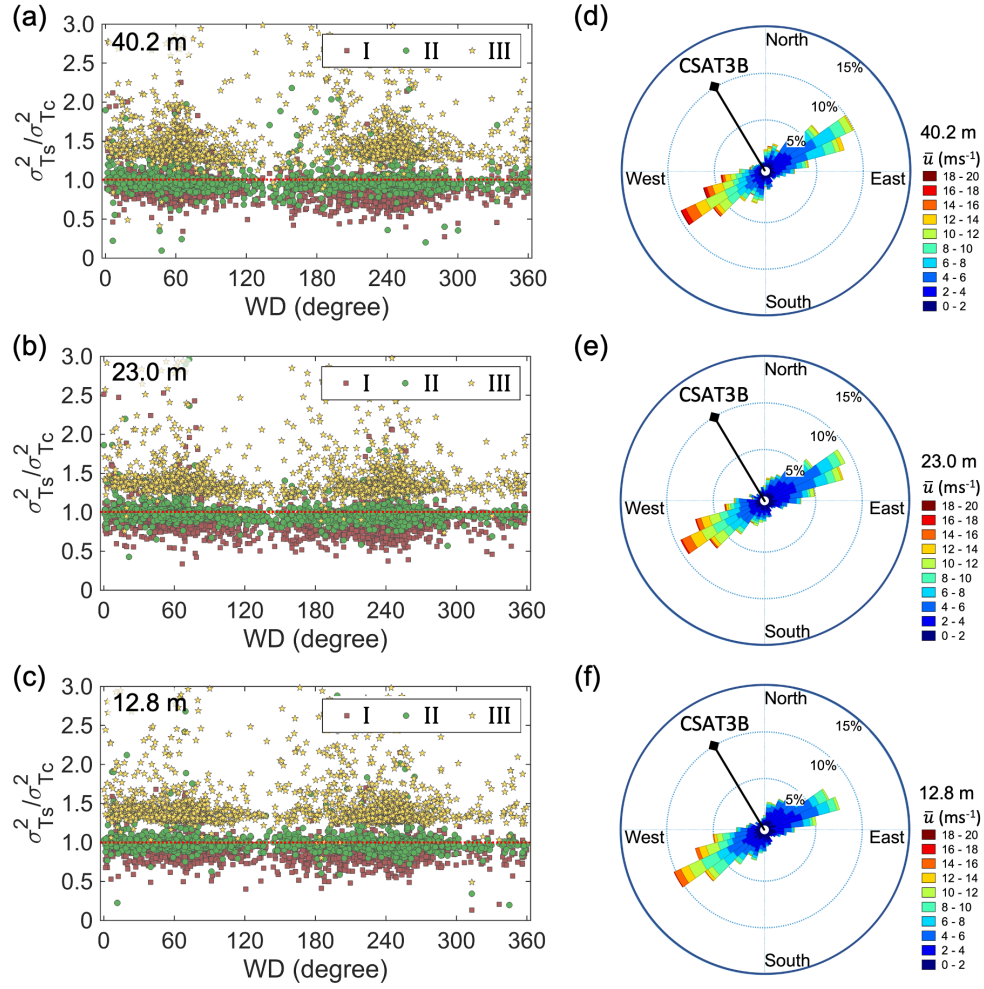
Figure 4. (a-c) Distribution of ratios of half-hourly variances of T_s and T_c with wind directions and (d-f) wind roses at the heights of 40.2, 23.0, and 12.8 m, respectively. The square, circle, and pentagram markers represent the ratios of the variances in the three frequency ranges. The black lines in d-f refer to directions of the mounting arms of instruments.

298
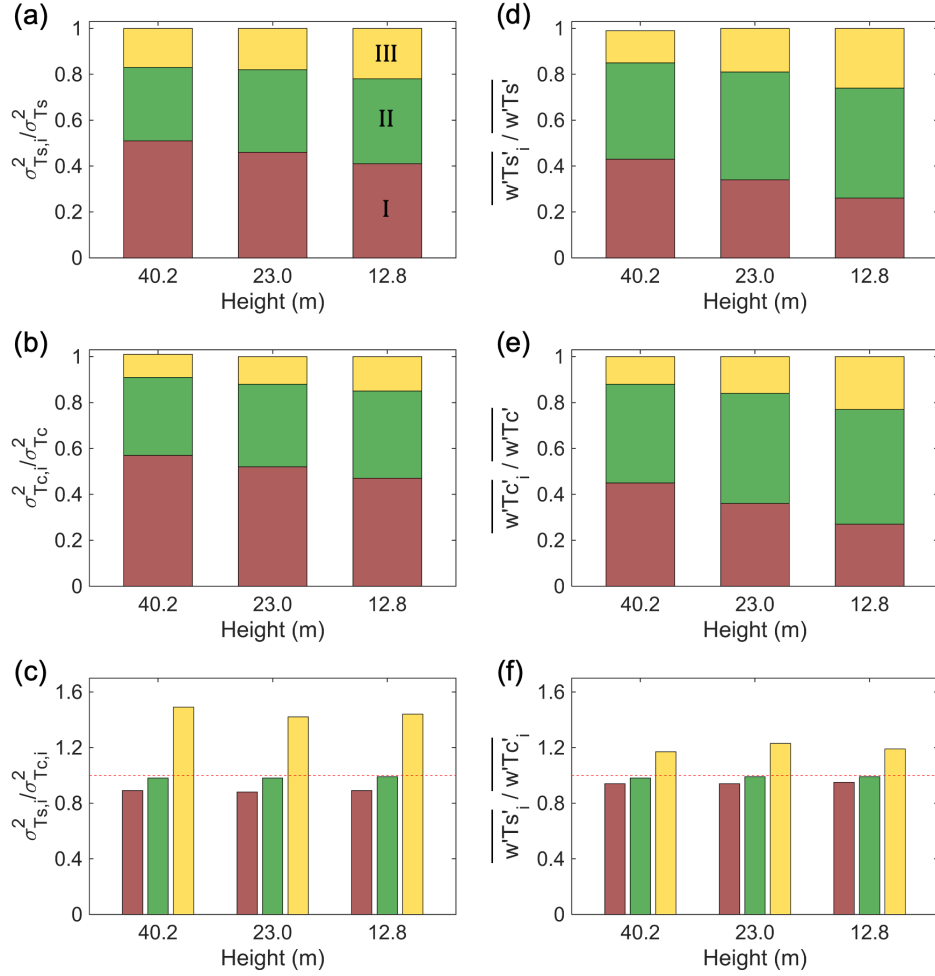
Figure 5. Contributions of the three frequency ranges to the total temperature variances and fluxes of T_s and T_c, respectively, as well as the mean ratios of the temperature variances and fluxes of T_s and T_c for each regime.

302

For regime II, the ratios between the variances of T_s and T_c and the associated fluxes are close to 1.0 with minimal scatter. This indicates that turbulent eddies with scales between 0.02 Hz and 0.2 Hz contribute consistently to the temperature variances and fluxes. These turbulent eddies contribute 32%–38% and 42%–50% to their total variances and fluxes, respectively (Figure 5 and Table 1). For regime III, the ratios between the variances of T_s and T_c average about 1.45 at the three heights due to the distorted spectra in this regime for both T_s and T_c. This indicates that turbulent eddies with scales larger than 0.2 Hz contribute roughly 45% less to $\sigma^2_{T_{c,III}}$ than $\sigma^2_{T_{s,III}}$. With these turbulent eddies contributing about 12%–26% to the total variances (Figures 5a-5c and Table 1), the 45% difference in $\sigma^2_{T_{c,III}}$ and $\sigma^2_{T_{s,III}}$ would cause 5%–7% difference in the total

312   variances of T_s and T_c. As for fluxes, turbulent eddies with scales larger than 0.2 Hz contribute

313   approximately 20% less to $\overline{w'T_c'}_{III}$ than $\overline{w'T_s'}_{III}$. With these turbulent eddies accounting for 12%–

314   26% of the total fluxes (Figures 5d-5f and Table 1), the 20% difference in $\overline{w'T_c'}_{III}$ and $\overline{w'T_s'}_{III}$

315   would cause 2%–4% difference in the total fluxes. These results suggest that the observed

316   underestimation of the T_s variances and fluxes is primarily attributed to the large turbulent eddies

317   with frequencies less than 0.02 Hz, which is offset to some extent by the contribution from small

318   turbulent eddies with frequencies larger than 0.2 Hz.

319

320   **3.4 Potential causes for the scale-dependent differences**

321   The potential causes for the scale-dependent differences between the T_s and T_c spectra

322   include measurement errors, solar heating of thermocouples, and tower and mounting arm

323   vibrations, among others (e.g., the deficiency in the design of sonic anemometers in response to

324   different wind speed conditions). The T_c spectra follow similar declining features in the high

325   frequency range independent to wind speed (Text S2 and Figure S2), suggesting that

326   measurements of the fine-wire thermocouples were not noticeably affected by increased wind

327   speed, and therefore operational errors could be excluded from the causes for the observed

328   difference. Additionally, the consistent differences between the power spectra of T_s and T_c under

329   nighttime and daytime conditions (Text S1 and Figure S1) suggest that the impact of solar heating

330   on thermocouples was also not the cause for the differences between the T_s and T_c variances and

331   fluxes.

332   As the wind speed increases, the tower vibrations become more pronounced, especially at

333   higher levels, as indicated by the more energetic peaks in the power spectra of sonic roll and pitch

334   angles (Figure 6). For wind speed below approximately 10 m s^{-1} at 40.2 m, the ratios of the T_s and

335   T_c variances for regime I show no obvious change with wind speed. However, for wind speed

336   above 10 m s^{-1}, the ratios decrease further as wind speed increases (Figure 7a). The ratios of the

337   temperature fluxes of T_s and T_c exhibit a similar pattern to the variances (Figure 7d). For regime

338   II, the ratios of both the variance and fluxes of T_s and T_c show no obvious relations with wind

339   speed (Figures 7b and 7e). For regime III, the ratios of both the variance and fluxes of T_s and T_c

340   illustrate large scatter, especially when wind speed is below 10 m s^{-1}, but still show no obvious

341   trends as wind speed increases (Figures 7c and 7f).
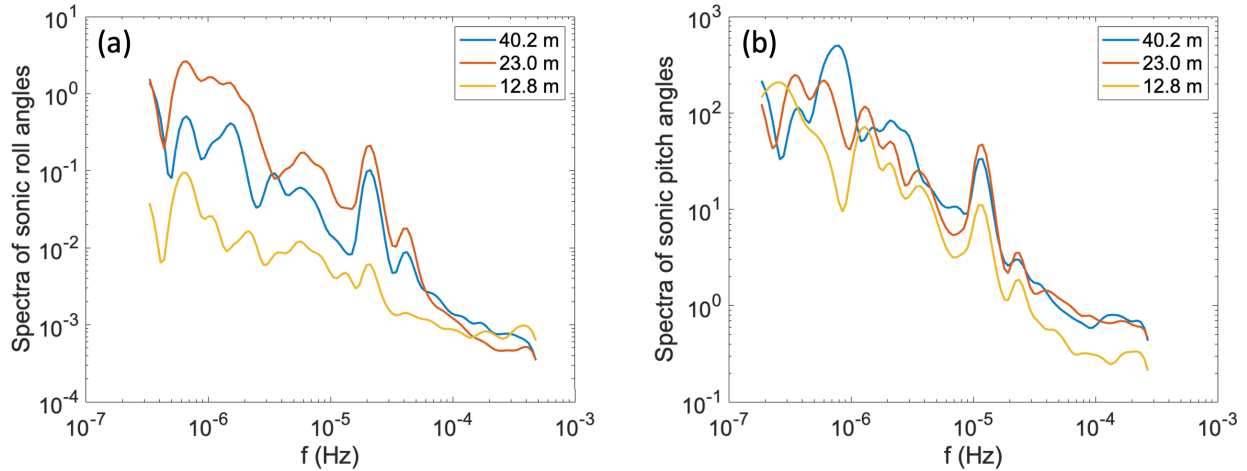
Figure 6. Power spectra of the sonic (a) roll and (b) pitch angles measured by CSAT3B at the three heights. The sonic roll and pitch angles were stored as 30-min averages during the experiment.

We thus hypothesize that the enhanced tower vibrations under strong winds lead to an early or delayed detection of the sonic pulse. This results in overestimations or underestimations of the speed of sound and thus errors in the 10 Hz time series of sonic temperature. In this study, for wind speeds below 10 m s^{-1}, the ratios of the variances (and fluxes) of T_s to those of T_c are scattered around 1.0 for regime I. However, for wind speed above 10 m s^{-1}, the ratios decrease as wind speed further increases (Figure 7). Therefore, tower and mounting arm vibrations were most likely the cause for the differences in the temperature variance and fluxes. Under this circumstance, such vibrations may also affect sonic-measured wind components along with T_s, resulting in errors in all the calculated fluxes. However, rigorous tests of this hypothesis seem necessary through testing sonic anemometers in wind tunnels or fields with different mounting strategies.

357
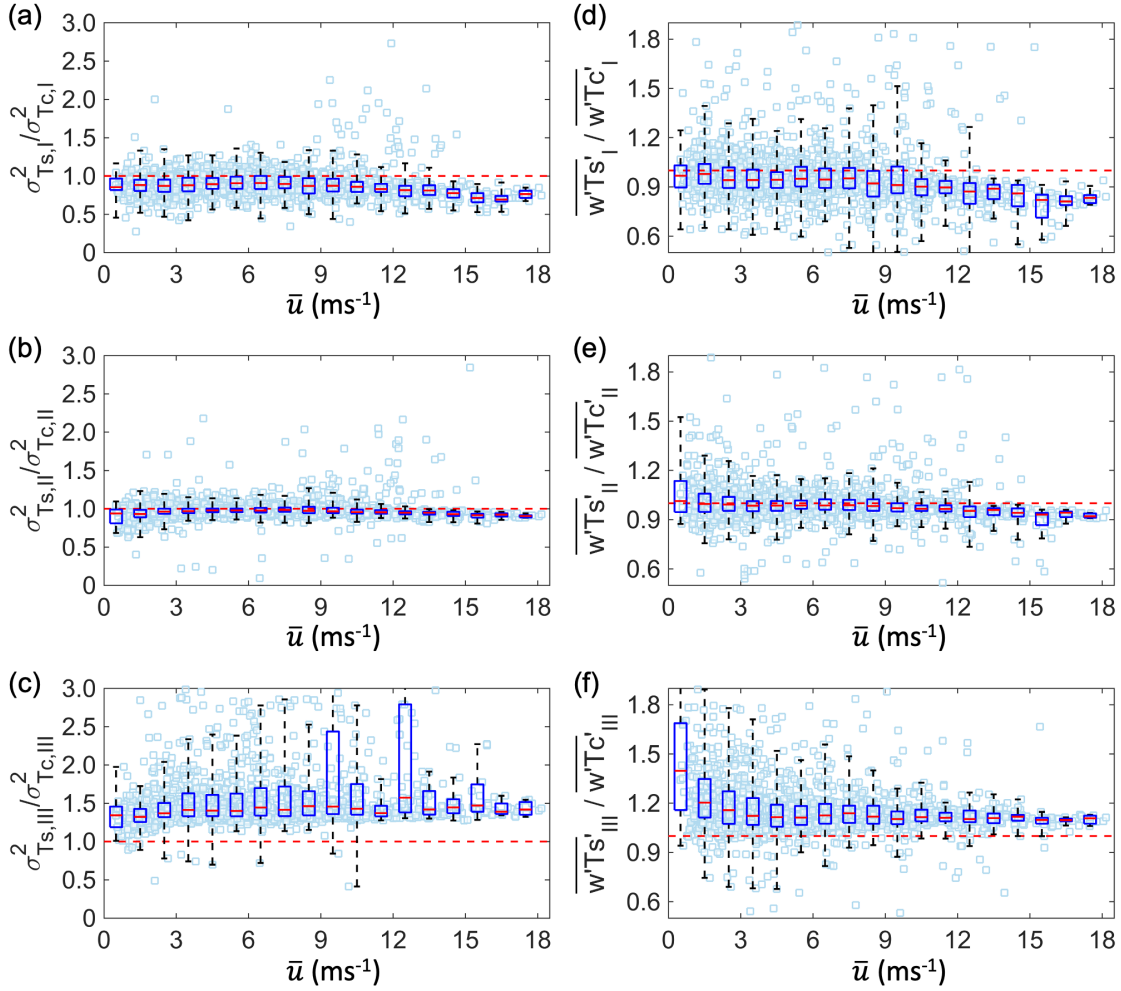
Figure 7. Ratios of (a, b, and c) half-hourly variances of T_s and T_c and (d, e, and f) covariances of w-T_s and w-T_c corresponding to the low, middle, and high frequency ranges, respectively, as a function of the mean wind speed ($\bar{u}$) at 40.2 m.

361

3.5 Implications to water vapor and CO₂ fluxes

Given that equations (2) and (3) are used to adjust the measured densities of water vapor and CO_2 by open-path CO_2/H_2O gas analyzers in EC systems, any errors in temperature measurements would be propagated to water vapor and CO_2 time series through these two equations. In equations (2) and (3), T_s can be replaced by T_c to achieve the adjusted time series of densities of water vapor and CO_2 for FW3. The adjusted time series of water vapor and CO_2 by the fluctuating parts of T_s and T_c, respectively, are then decomposed into three frequency ranges to quantify the influence of T_s on variances and fluxes of water vapor and CO_2.

370   The variances of ρ_v are not influenced by using either T_s or T_c for the density effect
371   corrections (Table S1) because the fluctuations in ρ_v are not very sensitive to the density effects,
372   especially at semiarid sites like ours (Gao et al., 2020). Therefore, for the water vapor fluxes, there
373   only exist minor differences (< 1%) between the fluxes corrected by T_s and T_c for the three
374   frequency ranges, while the overall water vapor fluxes corrected by T_s and T_c are comparable at
375   the three heights (Figures 8a-8c).
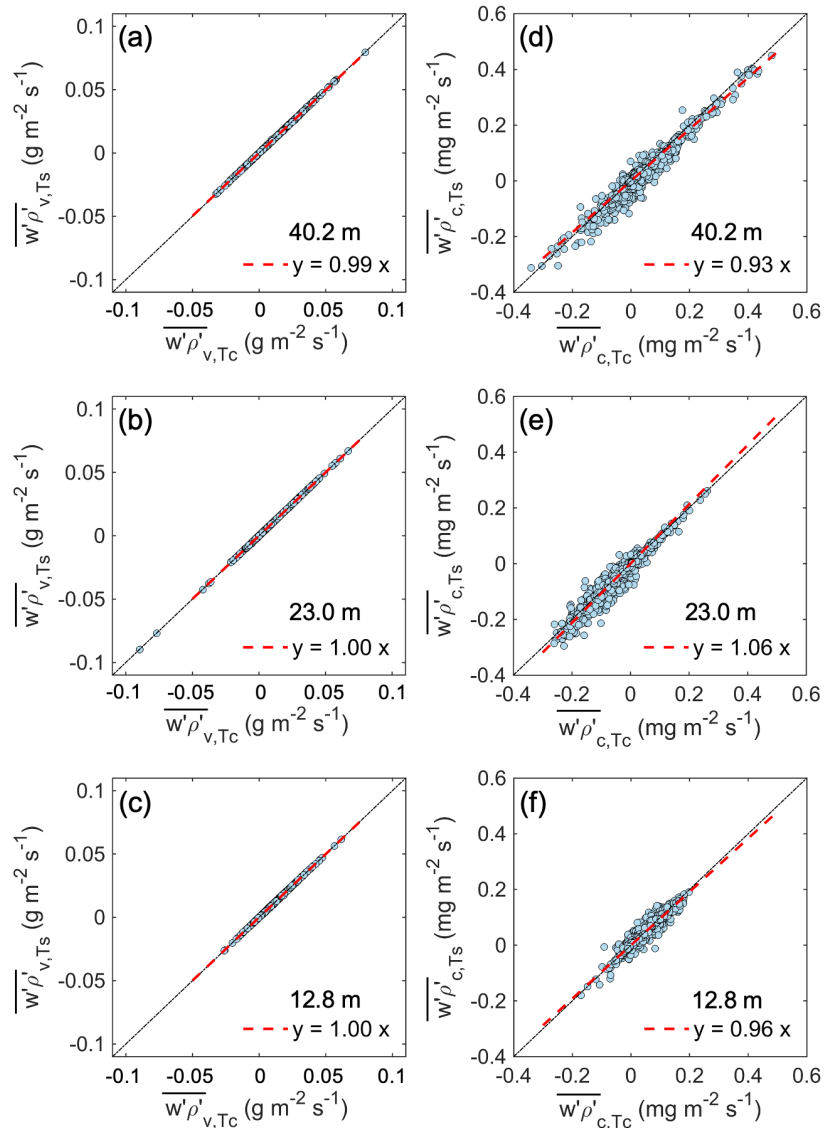
376

377   **Figure 8.** Comparison of water vapor and CO_2 fluxes corrected by temperature from sonic
378   anemometers and fine wire thermocouples, respectively, at the three heights.

379

380   As for CO_2, the differences between T_s and T_c in the three frequency ranges are propagated

381   differently to the adjusted variances of ρ_c (Table S2). More importantly, there exist relatively large

382   differences (but still within 10%) between the CO_2 fluxes adjusted by T_s and T_c (Figures 8d-8f).

383   In general, CO_2 fluxes are more sensitive to errors or uncertainties in temperature measurements

384   than water vapor fluxes (Liu et al., 2006). Therefore, precise measurements of air temperature are

385   critical for quantifying ecosystem CO_2 fluxes.

386

387

388   **4 Conclusions**

389   Temperature variances and the associated fluxes are examined by using sonic anemometers

390   and co-located fine-wire thermocouples at three levels above a sagebrush ecosystem. Compared

391   to temperature variances and fluxes determined by thermocouples, sonic anemometers were found

392   to underestimate the variances and fluxes by approximately 5% and 4%, respectively, at the height

393   of 40.2 m. In the high frequency range, the distortion in T_s spectra contributed to the heat fluxes

394   by 2–4%, whereas the attenuation in T_c spectra led to underestimated fluxes. However, the primary

395   source of the underestimation in temperature variances and fluxes by the sonic anemometers was

396   identified in the low frequency range. This phenomenon became more profound with increasing

397   wind speed, and thus, heightened vibrations of the tower and mounting arms. Furthermore, when

398   adjusting the density effects using the attenuated temperature, our results indicate that CO_2

399   variances and fluxes are more sensitive to errors or uncertainties in temperature measurements

400   compared to those of water vapor at the semiarid site.

401   Our findings highlight the critical importance of accurate measurements of air temperature

402   fluctuations in EC flux measurements. The inclusion of additional high-frequency temperature

403   measurements using fine-wire thermocouples is thus strongly recommended for EC systems.

404   Furthermore, the observed underestimation of sonic temperature variances and fluxes suggests that

405   the measured wind velocity components may also be biased due to the tower vibrations. Therefore,

406   we recommend further investigation of the influence of mounting arm vibrations on wind velocity

407   components by sonic anemometers.

408

409   **Data availability**

410   The data used in this study are available from Heping Liu upon request.

411

Code availability

The code used in this study are available from Zhongming Gao and Heping Liu upon request.

412
413
414
415

Author contributions

ZG and HL designed the study with substantial input from all coauthors. ZG, HL, DL, and BY conducted the fieldwork and obtained and processed the EC data. ZG drafted the manuscript. All authors contributed to the result analysis and interpretation, commented on and approved the final paper.

416
417
418
419
420
421

Competing Interests

The authors declare that they have no known competing financial interests or personal relationships that could have appeared to influence the work reported in this paper.

422
423
424
425

Acknowledgments

We thank Patrick O'Keeffe, Dennis Finn, Jason Rich, and Matthew S. Roetcisoender for their assistance in the lab and field. This work was supported by the National Natural Science Foundation of China (U21A6001), the Fundamental Research Funds for the Central Universities, Sun Yat-sen University (23ptpy91), and the National Science Foundation (NSF-AGS-1419614, NSF-AGS-1853050, NSF-AGS-1853354).

426
427
428
429
430
431
432
433

References

Burns, S. P., Horst, T. W., Jacobsen, L., Blanken, P. D. and Monson, R. K.: Using sonic anemometer temperature to measure sensible heat flux in strong winds, Atmos. Meas. Tech., 5(9), 2095–2111, doi:10.5194/AMT-5-2095-2012, 2012.

Chu, H., Luo, X., Ouyang, Z., Chan, W. S., Dengel, S., Biraud, S. C., Torn, M. S., Metzger, S., Kumar, J., Arain, M. A., Arkebauer, T. J., Baldocchi, D., Bernacchi, C., Billesbach, D., Black, T. A., Blanken, P. D., Bohrer, G., Bracho, R., Brown, S., Brunsell, N. A., Chen, J., Chen, X., Clark, K., Desai, A. R., Duman, T., Durden, D., Fares, S., Forbrich, I., Gamon, J. A., Gough, C. M., Griffis, T., Helbig, M., Hollinger, D., Humphreys, E., Ikawa, H., Iwata, H., Ju, Y., Knowles, J. F., Knox, S. H., Kobayashi, H., Kolb, T., Law, B., Lee, X., Litvak,

434
435
436
437
438
439
440
441
442
443

M., Liu, H., Munger, J. W., Noormets, A., Novick, K., Oberbauer, S. F., Oechel, W., Oikawa, P., Papuga, S. A., Pendall, E., Prajapati, P., Prueger, J., Quinton, W. L., Richardson, A. D., Russell, E. S., Scott, R. L., Starr, G., Staebler, R., Stoy, P. C., Stuart-Haëntjens, E., Sonnentag, O., Sullivan, R. C., Suyker, A., Ueyama, M., Vargas, R., Wood, J. D. and Zona, D.: Representativeness of Eddy-Covariance flux footprints for areas surrounding AmeriFlux sites, Agric. For. Meteorol., 301–302, 108350, doi:10.1016/J.AGRFORMET.2021.108350, 2021.

Detto, M. and Katul, G. G.: Simplified expressions for adjusting higher-order turbulent statistics obtained from open path gas analyzers, Boundary-Layer Meteorol., 122(1), 205–216, doi:10.1007/s10546-006-9105-1, 2007.

Eder, F., Serafimovich, A. and Foken, T.: Coherent Structures at a Forest Edge: Properties, Coupling and Impact of Secondary Circulations, Boundary-Layer Meteorol., 148(2), 285–308, doi:10.1007/s10546-013-9815-0, 2013.

Finn, D., Clawson, K. L., Eckman, R. M., Liu, H., Russell, E. S., Gao, Z. and Brooks, S.: Project sagebrush: Revisiting the value of the horizontal plume spread parameter σy, J. Appl. Meteorol. Climatol., 55(6), 1305–1322, doi:10.1175/JAMC-D-15-0283.1, 2016.

Finn, D., Eckman, R. M., Gao, Z. and Liu, H.: Mechanisms for wind direction changes in the very stable boundary layer, J. Appl. Meteorol. Climatol., 57(11), 2623–2637, doi:10.1175/JAMC-D-18-0065.1, 2018.

Frank, J. M., Massman, W. J. and Ewers, B. E.: Underestimates of sensible heat flux due to vertical velocity measurement errors in non-orthogonal sonic anemometers, Agric. For. Meteorol., 171–172, 72–81, doi:10.1016/J.AGRFORMET.2012.11.005, 2013.

Fratini, G., Ibrom, A., Arriga, N., Burba, G. and Papale, D.: Relative humidity effects on water vapour fluxes measured with closed-path eddy-covariance systems with short sampling lines, Agric. For. Meteorol., 165, 53–63, doi:10.1016/J.AGRFORMET.2012.05.018, 2012.

Gao, Z., Liu, H., Li, D., Katul, G. G. and Blanken, P. D.: Enhanced Temperature-Humidity Similarity Caused by Entrainment Processes With Increased Wind Shear, J. Geophys. Res. Atmos., 123(8), 4110–4121, doi:10.1029/2017JD028195, 2018.

Gao, Z., Liu, H., Arntzen, E., Mcfarland, D. P., Chen, X. and Huang, M.: Uncertainties in Turbulent Statistics and Fluxes of CO_2 Associated With Density Effect Corrections, Geophys. Res. Lett., 47(15), doi:10.1029/2020GL088859, 2020.

Guo, X., Zhang, H., Cai, X., Kang, L., Zhu, T. and Leclerc, M.: Flux-Variance Method for Latent Heat and Carbon Dioxide Fluxes in Unstable Conditions, Boundary-Layer Meteorol., 131(3), 363–384, doi:10.1007/s10546-009-9377-3, 2009.

Hong, J., Kim, J., Ishikawa, H. and Ma, Y.: Surface layer similarity in the nocturnal boundary layer: the application of Hilbert-Huang transform, Biogeosciences, 7(4), 1271–1278, doi:10.5194/bg-7-1271-2010, 2010.

Horst, T. W., Semmer, S. R. and Maclean, G.: Correction of a Non-orthogonal, Three-Component Sonic Anemometer for Flow Distortion by Transducer Shadowing, Boundary-Layer Meteorol., 155(3), 371–395, doi:10.1007/S10546-015-0010-3, 2015.

Huang, N. E. and Wu, Z.: A review on Hilbert-Huang transform: Method and its applications to geophysical studies, Rev. Geophys., 46(2), RG2006, doi:10.1029/2007RG000228, 2008.

Huang, N. E., Shen, Z., Long, S. R., Wu, M. C., Shih, H. H., Zheng, Q., Yen, N.-C., Tung, C. C. and Liu, H. H.: The empirical mode decomposition and the Hilbert spectrum for nonlinear and non-stationary time series analysis, Proc. R. Soc. London A Math. Phys. Eng. Sci., 454(1971), 903–995, doi:10.1098/rspa.1998.0193, 1998.

Kaimal, J. C., Finnigan, J. J.: Atmospheric boundary layer flows: their structure and measurement, Oxford Univ. Press, New York, 1994

Lan, C., Liu, H., Li, D., Katul, G. G. and Finn, D.: Distinct Turbulence Structures in Stably Stratified Boundary Layers With Weak and Strong Surface Shear, J. Geophys. Res. Atmos., 123(15), 7839–7854, doi:10.1029/2018JD028628, 2018.

Lee, X. and Massman, W.: A Perspective on Thirty Years of the Webb, Pearman and Leuning Density Corrections, Boundary-Layer Meteorol., 139(1), 37–59, doi:10.1007/s10546-010-9575-z, 2011.

Lee, X., Liu, S., Xiao, W., Wang, W., Gao, Z., Cao, C., Hu, C., Hu, Z., Shen, S., Wang, Y., Wen, X., Xiao, Q., Xu, J., Yang, J. and Zhang, M.: The Taihu Eddy Flux Network: An Observational Program on Energy, Water, and Greenhouse Gas Fluxes of a Large Freshwater Lake, Bull. Am. Meteorol. Soc., 95(10), 1583–1594, doi:10.1175/BAMS-D-13-00136.1, 2014.

Li, D., Katul, G. G. and Liu, H.: Intrinsic Constraints on Asymmetric Turbulent Transport of Scalars Within the Constant Flux Layer of the Lower Atmosphere, Geophys. Res. Lett., 45(4), 2022–2030, doi:doi/10.1002/2018GL077021, 2018.

Liu, H., Peters, G. and Foken, T.: New equations for sonic temperature variance and buoyancy heat flux with an omnidirectional sonic anemometer, Boundary-Layer Meteorol., 100(3), 459–468, doi:10.1023/A:1019207031397, 2001.

Liu, H., Randerson, J., Lindfors, J., Massman, W. and Foken, T.: Consequences of Incomplete Surface Energy Balance Closure for CO_2 Fluxes from Open-Path CO_2/H_2O Infrared Gas Analysers, Boundary-Layer Meteorol., 120(1), 65–85, doi:10.1007/s10546-005-9047-z, 2006.

Liu, H., Gao, Z. and Katul, G. G.: Non-Closure of Surface Energy Balance Linked to Asymmetric Turbulent Transport of Scalars by Large Eddies, J. Geophys. Res. Atmos., 126(7), e2020JD034474, doi:10.1029/2020JD034474, 2021.

Loescher, H. W., Ocheltree, T., Tanner, B., Swiatek, E., Dano, B., Wong, J., Zimmerman, G., Campbell, J., Stock, C., Jacobsen, L., Shiga, Y., Kollas, J., Liburdy, J. and Law, B. E.: Comparison of temperature and wind statistics in contrasting environments among different sonic anemometer-thermometers, Agric. For. Meteorol., 133(1–4), 119–139, doi:10.1016/J.AGRFORMET.2005.08.009, 2005.

Massman, W. and Clement, R.: Uncertainty in Eddy Covariance Flux Estimates Resulting from Spectral Attenuation, Handb. Micrometeorology, 67–99, doi:10.1007/1-4020-2265-4_4, 2006.

524   Mauder, M. and Zeeman, M. J.: Field intercomparison of prevailing sonic anemometers, Atmos.
525   Meas. Tech., 11(1), 249–263, doi:10.5194/amt-11-249-2018, 2018.

526   Mauder, M., Oncley, S. P., Vogt, R., Weidinger, T., Ribeiro, L., Bernhofer, C., Foken, T.,
527   Kohsiek, W., De Bruin, H. A. R. and Liu, H.: The energy balance experiment EBEX-2000.
528   Part II: Intercomparison of eddy-covariance sensors and post-field data processing methods,
529   Boundary-Layer Meteorol., 123(1), 29–54, doi:10.1007/s10546-006-9139-4, 2007.

530   Mauder, M., Foken, T. and Cuxart, J.: Surface-Energy-Balance Closure over Land: A Review,
531   Boundary-Layer Meteorol., 177(2–3), 395–426, doi:10.1007/s10546-020-00529-6, 2020.

532   Missik, J. E. C., Liu, H., Gao, Z., Huang, M., Chen, X., Arntzen, E., Mcfarland, D. P. and
533   Verbeke, B.: Groundwater Regulates Interannual Variations in Evapotranspiration in a
534   Riparian Semiarid Ecosystem, J. Geophys. Res. Atmos., 126(7), e2020JD033078,
535   doi:10.1029/2020jd033078, 2021.

536   Peña, A., Dellwik, E. and Mann, J.: A method to assess the accuracy of sonic anemometer
537   measurements, Atmos. Meas. Tech., 12(1), 237–252, doi:10.5194/AMT-12-237-2019,
538   2019.

539   Sahlée, E., Smedman, A.-S., Rutgersson, A. and Högström, U.: Spectra of CO_2 and Water
540   Vapour in the Marine Atmospheric Surface Layer, Boundary-Layer Meteorol., 126(2), 279–
541   295, doi:10.1007/s10546-007-9230-5, 2008.

542   Schotanus, P., Nieuwstadt, F. T. M. and De Bruin, H. A. R.: Temperature measurement with a
543   sonic anemometer and its application to heat and moisture fluxes, Boundary-Layer
544   Meteorol., 26(1), 81–93, doi:10.1007/BF00164332, 1983.

545   Smedman, A., Högström, U., Sahlée, E. and Johnson, C.: Critical re-evaluation of the bulk
546   transfer coefficient for sensible heat over the ocean during unstable and neutral conditions,
547   Q. J. R. Meteorol. Soc., 133(622), 227–250, doi:10.1002/qj.6, 2007.

548   Stull, R. B.: An Introduction to Boundary Layer Meteorology, Kluwer Academic Publishers,
549   Dordrecht, Netherlands., 1988.

550   Tang, S., Xie, S., Zhang, M., Tang, Q., Zhang, Y., Klein, S. A., Cook, D. R. and Sullivan, R. C.:
551   Differences in Eddy-Correlation and Energy-Balance Surface Turbulent Heat Flux
552   Measurements and Their Impacts on the Large-Scale Forcing Fields at the ARM SGP Site,
553   J. Geophys. Res. Atmos., 124(6), 3301–3318, doi:10.1029/2018JD029689, 2019.

554   Wang, G., Huang, J., Guo, W., Zuo, J., Wang, J., Bi, J., Huang, Z. and Shi, J.: Observation
555   analysis of land-atmosphere interactions over the Loess Plateau of northwest China, J.
556   Geophys. Res., 115(D00K17), doi:10.1029/2009JD013372, 2010.

557   Webb, E. K., Pearman, G. I. and Leuning, R.: Correction of flux measurements for density
558   effects due to heat and water vapour transfer, Q. J. R. Meteorol. Soc., 106(447), 85–100,
559   doi:10.1002/qj.49710644707, 1980.

560   Wilczak, J. M., Oncley, S. P. and Stage, S. A.: Sonic Anemometer Tilt Correction Algorithms,
561   Boundary-Layer Meteorol., 99(1), 127–150, doi:10.1023/A:1018966204465, 2001.

562   Zhang, Y., Liu, H., Foken, T., Williams, Q., Liu, S., Mauder, M. and Liebethal, C.: Turbulence
563   Spectra and Cospectra Under the Influence of Large Eddies in the Energy Balance

564   EXperiment (EBEX), Boundary-Layer Meteorol., 136(2), 235–251, doi:10.1007/s10546-

565   010-9504-1, 2010.

566 Zhang, Y., Liu, H., Foken, T., Williams, Q., Mauder, M. and Thomas, C.: Coherent structures

567   and flux contribution over an inhomogeneously irrigated cotton field, Theor. Appl.

568   Climatol., 103(1–2), 119–131, doi:10.1007/s00704-010-0287-6, 2011.

569

570